

## Article

# UV Resistance of Super-Hydrophobic Stainless Steel Surfaces Textured by Femtosecond Laser Pulses

Oleksiy Myronyuk <sup>1</sup>, Denys Baklan <sup>1</sup> and Aleksej M. Rodin <sup>2,\*</sup>

<sup>1</sup> Department of Chemical Technology of Composite Materials, Chemical Technology Faculty, Igor Sikorsky Kyiv Polytechnic Institute, Beresteyskiy Ave. 37, 03056 Kyiv, Ukraine; o.myronyuk@kpi.ua (O.M.); d.baklan@kpi.ua (D.B.)

<sup>2</sup> Solid State Laser Laboratory, Department of Laser Technologies, Center for Physical Sciences and Technology, Savanoriu Ave. 231, 02300 Vilnius, Lithuania

\* Correspondence: aleksej.rodin@ftmc.lt; Tel.: +370-60140057

**Abstract:** The loss of spontaneous liquid repellency on the surface of AISI 304 stainless steel under UV irradiation has been investigated depending on the textures formed by femtosecond laser pulses using Owens–Wendt plot analysis. Laser-induced periodic surface structures (LIPSS) have shown less liquid repellency compared to microgrooves. The polarity of the super-hydrophobic non-polar layer increased under UV irradiation to a super-hydrophilic state. The rate of this transition is determined by the surface topography and was faster for LIPSS compared to the bihierarchical textures formed by LIPSS in combination with microgrooves. The applicability of the Owens–Wendt approach for the numerical comparison of the achievable liquid repellency of textured surfaces in the Cassie state and the degree of polarity reversal of the hydrophobic layer was shown.

**Keywords:** UV irradiation; functional materials; superhydrophobic surface; LIPSS; laser micro-texturing; contact angle; Owens–Wendt approach



**Citation:** Myronyuk, O.; Baklan, D.; Rodin, A.M. UV Resistance of Super-Hydrophobic Stainless Steel Surfaces Textured by Femtosecond Laser Pulses. *Photonics* **2023**, *10*, 1005. <https://doi.org/10.3390/photonics10091005>

Received: 27 July 2023

Revised: 30 August 2023

Accepted: 1 September 2023

Published: 3 September 2023



**Copyright:** © 2023 by the authors. Licensee MDPI, Basel, Switzerland. This article is an open access article distributed under the terms and conditions of the Creative Commons Attribution (CC BY) license (<https://creativecommons.org/licenses/by/4.0/>).

## 1. Introduction

The exceptional water repellency inherent in many natural surfaces, such as lotus petals and the shells of some insects, served as an example for the study of artificial bioinspired surfaces of this class [1]. Water wetting is often critical for such natural surfaces. For example, the surface tension of water is a lethal force for light insects. Therefore, a water-repellency mechanism has evolved in the course of evolution based on a special surface texture and a reduced surface energy of the material. The first factor was implemented due to special villi or outgrowths, and the second due to waxy substances with low polarity, causing an increase in the wetting angle with polar liquids, such as water. The same principle is now in the spotlight of synthetic materials development. Increased water repellency is highly desirable for anti-icing, self-cleaning, antibacterial, anti-corrosion, and oil-cleaning properties [2].

To date, various methods have been developed for obtaining surface textures, including chemical vapor deposition [3–5], electrochemical deposition [6,7], and layer-by-layer deposition [8–12]. However, the inherent disadvantages were poor scalability and the high cost of surface modification [13]. Laser processing has proven to be a promising way to solve these problems in the surface texturing of materials [14,15], such as structural metals. It is known [16,17] that ablation of a metal surface by femtosecond laser pulses is the least destructive method due to the short interaction time. This makes it possible to reproduce not only micron but also submicron patterns [18,19] formed by laser-induced periodic surface structures (LIPSS). The successful formation of such patterns on steel to control wetting was demonstrated in [20], and the dependence of water repellency on microstructure parameters (line-to-line spacing) was studied in [21]. Micropatterns in combination with LIPSS were considered in [22]. The material of these textures was subjected to additional

hydrophobization to reduce the surface energy [23], which ensured a contact angle of more than  $150^\circ$ , corresponding to the super-hydrophobic state [24]. To reduce the surface energy of such textures, chemical vapor deposition [25] or wet chemical treatment [26] can be used.

The phenomenon of spontaneous hydrophobization that occurs on metal surfaces is also known [27]. Prolonged exposure to ambient air leads to spontaneous hydrophobization with a water contact angle of more than  $155^\circ$  [28] due to the action of water [29], hydrocarbons [30], and carbon dioxide [31–33]. Nevertheless, the observed decrease in the surface polarity [34] remains unclear. A hydrophobic layer was formed even in a vacuum [35] and remained after treatment with a solvent [36]. This effect has great potential in terms of eliminating the need for post-treatment. However, a thin organic layer is vulnerable to high-energy solar UV photons [37], which may limit the outdoor stability of such surfaces. On the other hand, self-hydrophobization is undesirable in other applications where increased wettability is required, or post-treatment is expected. Therefore, the study of the wetting stability of self-hydrophobized femtosecond-laser-textured surfaces under UV irradiation is of great importance for improving the liquid-repellent properties and cleaning the surface.

The main indicator for evaluating the water-repellent properties of textured surfaces is usually the static contact angle, although the hysteresis of the contact angle, the advancing and receding angles, and the sliding angle are also used [38]. In some studies, the bouncing droplet technique is used to assess the wetting dynamics [39]. The goal of the current study was to characterize the stability of a spontaneous hydrophobized layer on the surface of widely used AISI 304 stainless steel [40,41] under UV irradiation with respect to a pattern textured by femtosecond laser pulses. Accordingly, an adapted Owens–Wendt approach was chosen as a tool to characterize the change in surface energy during photodegradation. Its sensitivity to the polarity of the material of textured surfaces has already been shown [42].

## 2. Materials and Methods

### 2.1. Sample Processing

Both LIPSS patterns and microgrooves were formed with an air-cooled femtosecond laser (Carbide from Light Conversion, Vilnius, Lithuania) on a smooth surface of  $20 \times 20 \text{ mm}^2$  AISI 304 stainless steel specimens 2 mm thick. Prior to laser processing, metal surfaces were degreased and cleaned with isopropyl alcohol. When operating at a repetition rate of 60 kHz, the average laser power was limited to  $\sim 3 \text{ W}$  at a fundamental wavelength of 1030 nm, and the pulse width was  $\sim 360 \text{ fs}$ . All textures were processed at a sample speed of 60 mm/s using X-Y precision linear stages (lower PRO165LM-0500 and upper PRO165LM-0300 from Aerotech, Inc., Pittsburgh, PA, USA). The definition of “sample speed” is identical to the more commonly used term “scanning speed” and is intended to clarify that instead of using a Galvo scanner, the sample was moved relative to the laser beam.

When forming LIPSS patterns, the laser beam was focused with a spot diameter of  $\sim 80 \mu\text{m}$  (at  $1/e^2$  level) onto the sample surface, and the pulse energy was  $46 \mu\text{J}$ , which corresponded to an energy density of  $\sim 0.9 \text{ J/cm}^2$ . The laser spots overlapped on the sample by 59% during continuous scanning and a step between adjacent passes of  $30 \mu\text{m}$ . A spherical lens with a focal length of 100 mm was used for focusing.

To engrave microgrooves, the output laser beam was expanded by a factor of 4 using a Galilean telescope and focused by a lens with a focal length of 1 inch into a spot with a diameter of  $\sim 5 \mu\text{m}$  (at  $1/e^2$  level). In this case, the laser pulse energy varied from  $21 \mu\text{J}$  to  $35 \mu\text{J}$ , which corresponded to the energy density from  $\sim 107 \text{ J/cm}^2$  to  $\sim 178 \text{ J/cm}^2$ . All microgrooves studied in this work were  $20 \mu\text{m}$  deep, which was achieved in 15 successive passes of the laser beam. Narrower grooves  $30 \mu\text{m}$  wide on samples “I” and “J” were machined at a laser pulse energy of  $21 \mu\text{J}$ , and grooves  $45 \mu\text{m}$  wide on samples “K” and “L” at an energy of  $35 \mu\text{J}$ , respectively. The laser-processing parameters (Table 1) were optimized for best performance and minimum sample contamination under laser power

and energy limitations. The experimental scheme was presented and described in more detail in a previous publication [43].

**Table 1.** Laser texturing parameters.

Parameter	LIPSS	Microgrooves
Average laser power	2.76 W	1.26 and 2.1 W
Laser wavelength		1030 nm
Laser repetition rate		60 kHz
Laser pulse width		~360 fs
Sample movement speed		60 mm/s
Beam spot diameter at $1/e^2$ level	~80 $\mu\text{m}$	~5 $\mu\text{m}$
Laser pulse energy	46 $\mu\text{J}$	21 and 35 $\mu\text{J}$
Energy density	~0.9 $\text{J}/\text{cm}^2$	107 and 178 $\text{J}/\text{cm}^2$

After laser texturing, the samples were sequentially washed in ultrasonic baths with distilled water and then with ethanol for 10 min and heated in an oven at 160 °C for 90 min. Then, the samples were stored for 3 months at a room temperature of 22 °C. A blank stainless steel sample (with a smooth, flat surface) was used as a reference.

## 2.2. Surface Characterization

The surface topography of textured samples was studied using a MIRA3 LMU scanning electron microscope (Tescan, s.r.o., Brno, Czech Republic). Contact angles were determined by the sessile drop technique using an optical microscope and H5D digital camera (Delta Optical, Shanghai, China) with “ScopeTek View” software (ScopeTek Optics Electronics, Hangzhou, China). Measurements were taken at five different spots on the sample surface. Drops with a volume of  $5 \pm 0.5 \mu\text{L}$  were applied to the surface with a micropipette at a temperature of 22 °C and a humidity of ~50%. After applying each probe liquid, the samples were dried in an oven for 1 min at a temperature of 60 °C. The contact angle was measured along the microgrooves. Water–ethanol mixtures were used as probe liquids to improve the measurement resolution. The surface tension values of the water–ethanol probe liquids were measured individually, and the decomposition was carried out by paraffin calibration. The surface tension of probe liquids was calculated from the dependences [44]. The elemental composition of the surface was determined using an INCA X-ACT X-ray energy dispersive spectrometer (EDS) (Oxford Instruments, Abingdon, UK). For each type of pattern, at least three measurements were taken on different areas of the textured surface. The elemental composition was calculated as an average value.

## 2.3. UV Resistance Testing

The method of UV surface aging was based on the assumption that during self-hydrophobization, an adsorbed organic layer is formed on the surface of the texture, which, due to its non-polarity, provides an increase in water repellency. Therefore, for accelerated aging of organic surfaces, the ASTM D 4329 process (cycle A) and the standard practice of ASTM G 154, which includes the use of a 400 W UVA 340 fluorescent lamp (with a wavelength of 340 nm and an irradiance of  $0.7 \text{ W}/\text{m}^2$ ) were chosen as the UV source. These standard procedures have been modified to eliminate the influence of environmental factors such as humidity and alternating dark/irradiation periods and focus only on surface-layer photoresistance. Since the lamp also emits in the IR range, to prevent heating of the surface of textured samples above 40 °C, the plates were placed on a steel substrate with a thermocouple. To ensure the stability of irradiation, the lamp was preheated for 5 min before loading the samples into the chamber. The distance between the sample and the UV lamp was 170 mm. The contact angle was measured after the samples were cooled to room temperature for 5 min (25 °C at 50% relative humidity).

### 2.4. Owens–Wendt Characterization Technique

The wetting process of the textured surfaces under consideration, which is affected by the roughness morphology, is described by the classical Wenzel (1) and Cassie (2) equations. These equations were used to predict the apparent surface contact angle  $\theta_A$  and its ratio to the intrinsic contact angle  $\theta$  for a chemically equivalent reference (flat) surface. For the Wenzel case, the liquid only contacts the solid surface, while in the case of Cassie, the air trapped in the texture creates a wetting state of the composite surface.

$$\cos\theta_A = r \cdot \cos\theta \tag{1}$$

where  $\theta_A$  is the contact angle of the liquid with the textured surface,  $\cos\theta$  is the contact angle of the equivalent reference (flat) surface, and  $r$  is the roughness, which is expressed as the ratio of the total surface area to the area of its projection.

$$\cos\theta_{\text{app}} = f_1 \cos\theta_1 + f_2 \cos\theta_2 \tag{2}$$

where  $\theta_{\text{app}}$  is the contact angle of a two-phase heterogeneous surface,  $\theta_A$  is the contact angle of the liquid with the surface texture,  $f_1$  and  $\cos\theta_1$  are the surface fraction and contact angle of the solid, and  $f_2$  and  $\cos\theta_2$  are the surface fraction and contact angle of the air, which is assumed to be  $360^\circ$ .

Thus, for the laser-processed surfaces with LIPSS patterns and microgrooves considered in the current work, increased wetting angles corresponding to the Wenzel and Cassie states are formed due to only partial contact of the probe liquid droplet with the surface. The contact fraction is determined both by the dimensions of the surface and its geometry.

The classical Owens–Wendt approach is based on the free surface energy equation [45] (3):

$$\sigma_{SL} = \sigma_S + \sigma_L - 2 \left( \sqrt{\sigma_S^D \sigma_L^D} + \sqrt{\sigma_S^P \sigma_L^P} \right) \tag{3}$$

where  $\sigma_{SL}$  is the surface energy at the solid–liquid interface,  $\sigma_S$  is the surface energy at the solid–air interface,  $\sigma_L$  is the surface tension of the liquid, and the indices  $D$  and  $P$  correspond to the dispersed and polar components of the surface energy. Combining this equation with Young’s equation and converting it to a linear form gives us the most practical Owens–Wendt Equation (4):

$$\frac{\sigma_L(1 + \cos\theta)}{2\sqrt{\sigma_L^D}} = \frac{\sqrt{\sigma_S^P} \sqrt{\sigma_L^P}}{\sqrt{\sigma_L^D}} + \sqrt{\sigma_S^D} \tag{4}$$

where  $\theta$  is the contact angle of the probe liquid (for certain  $\sigma_L$ ,  $\sigma_L^D$ , and  $\sigma_L^P$ ) with the tested surface.

Obviously, the classical approach does not take into account distortions caused by the surface roughness. However, such distortions of the classical linear form of the Owens–Wendt line can potentially serve as a tool for characterizing the Cassie state, the stability of surface wetting, and the boundaries of the wetting transition [42].

## 3. Results and Discussion

### 3.1. Features of the LIPSS Pattern and Microgrooves

The surface of the sample “H”, shown in Figure 1a, contains a LIPSS pattern with a pitch of approximately 150–250 nm. On the surface of samples “I”, “J”, and “K”, after the formation of a fine-scale LIPSS pattern identical to the sample “H”, microgrooves were processed. The parameters of the obtained large-scale and fine-scale textures on the steel surface are given in Table 2. Although samples “K” and “L” (Figure 2) appear to exhibit the same microtexture with a groove period of 60  $\mu\text{m}$  and a width of 45  $\mu\text{m}$ , sample “L”, nevertheless, does not contain a fine-scale LIPSS pattern on the top surface.

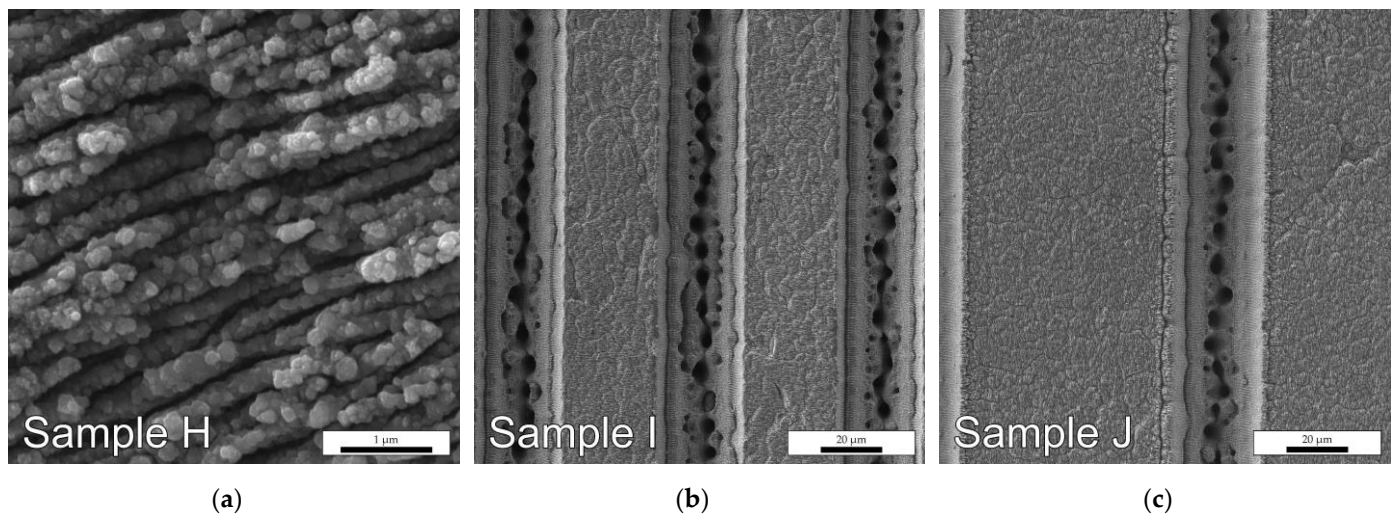


**Figure 1.** Sample surface topography under SEM: (a) LIPSS pattern on sample “H”; (b) LIPSS pattern and microgrooves with a period of 60  $\mu\text{m}$  and a width of 30  $\mu\text{m}$  on sample “I”; (c) LIPSS pattern and microgrooves with a period of 100  $\mu\text{m}$  and a width of 30  $\mu\text{m}$  on sample “J”.

**Table 2.** Texture parameters on the sample surface.

Sample	Microgrooves		Fine-Scale Pattern
Blank (reference)	–		–
H	–		LIPSS
I	Period 60 $\mu\text{m}$	Width 30 $\mu\text{m}$	LIPSS
J	Period 100 $\mu\text{m}$	Width 30 $\mu\text{m}$	LIPSS
K	Period 60 $\mu\text{m}$	Width 45 $\mu\text{m}$	LIPSS
L	Period 60 $\mu\text{m}$	Width 45 $\mu\text{m}$	–

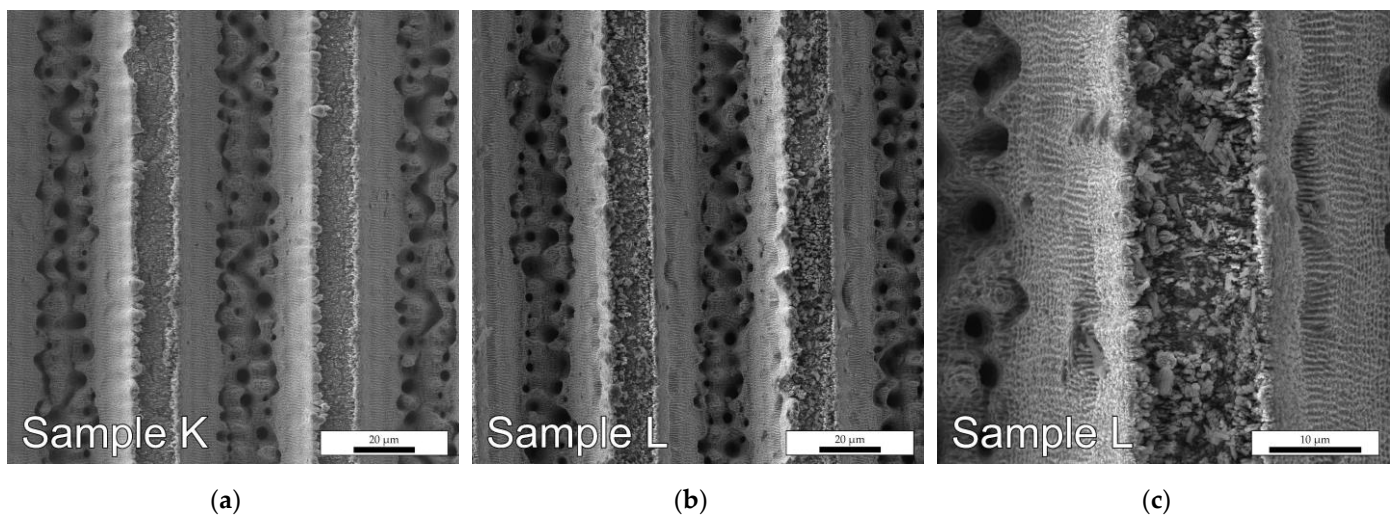


**Figure 2.** Sample surface topography under SEM: (a) LIPSS pattern and microgrooves with a period of 60  $\mu\text{m}$  and a width of 45  $\mu\text{m}$  on sample “K”; (b) microgrooves with a period of 60  $\mu\text{m}$  and a width of 45  $\mu\text{m}$  on sample “L”; (c) crystal-like texture on sample “L” at higher magnification.

At higher magnification (Figure 2c), on the side slopes of the grooves of the microtextured sample “L”, a fine-scale pattern is also visible, not as ordered as on the top surface of the sample “H” (Figure 1a). Such a grid-like pattern was explained by the defocusing of overlapping spots of the peripheral part of the laser beam after several successive passes when the laser-processing conditions approached those required for the formation

of LIPSS. [46]. Metal buildup was also observed along the edges of the groove, which increased the surface roughness. A significant difference between the topographies was crystal-like fragments embedded on the upper surface of sample “L” (Figure 2c), which could not be removed after washing in an ultrasonic bath. These random crystals were associated with the resolidification of evaporated metal on a smooth surface during laser ablation. Interestingly, the LIPSS pattern that formed on the surface of the “K” sample (Figure 3a) prevents the formation of such “acicular” textures.

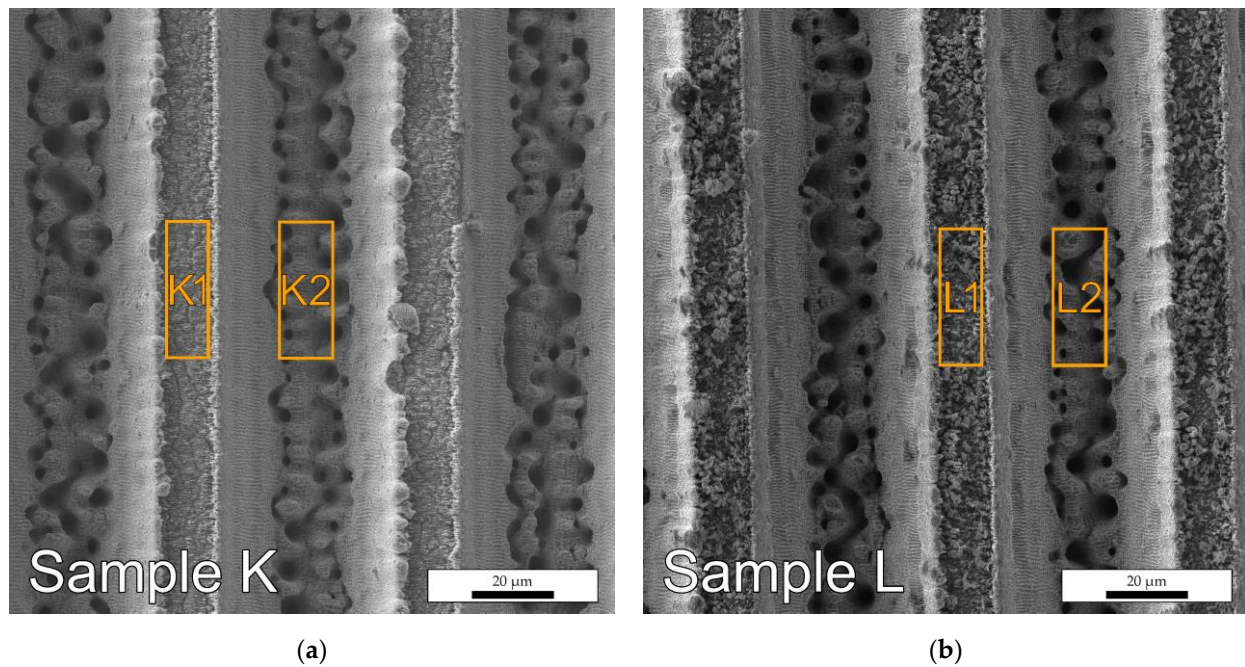


**Figure 3.** Texture scan areas for EDS analysis: (a) sample “K” and (b) sample “L”.

### 3.2. Surface Composition

According to the EDS analysis data (Figure 3 and Table 3), textured surfaces contain an increased amount of carbon compared to the reference (0.08% [47]). As mentioned above, this fact can be explained by the absorption of atmospheric carbon or other carbonaceous substances.

**Table 3.** EDS analysis of the content of elements in the sample textures (wt. %).

Area	C	O	Cr	Fe	Ni
K1	3.29	15.51	14.78	58.30	8.13
K2	3.28	3.45	19.37	66.37	7.54
L1	9.76	19.39	14.02	47.54	9.28
L2	4.38	3.94	18.21	68.23	5.24

The oxygen content is also higher than expected, which may be due to surface oxidation of the steel. Moreover, it can be seen that the protrusions (sections “K1” and “L1” in Figure 3) oxidized more noticeably than the grooves, probably due to the more developed specific surface area of these sections. Interestingly, oxygen content and carbon content are not related and, therefore, are not part of the same substance (probably an adsorbate). It is also worth noting that the carbon content in sample “L” is higher than in sample “K”, and on the protrusions, it is three times higher, which indicates greater contamination during spontaneous hydrophobization without a LIPSS pattern on the surface.

### 3.3. Wetting of Textured Surfaces

The static water contact angle for the obtained textures after spontaneous hydrophobization was in the range of 107–157° and significantly exceeded the figure for the reference sample of 71° (denoted in Figure 4 as flat steel—“Flat St”). Unexpectedly, the textures of samples “L” and “K” were the most effective, especially since the first did not contain an additional LIPSS pattern. This may be partly due to the formation of elevations along the edges of the protrusions visible in Figure 3 and the “acicular” crystal-like texture embedded into the surface of the sample “L” (Figure 2c). Sample “H”, containing only the LIPSS pattern, shows the lowest static water contact angle. UV irradiation leads to the loss of water-repellent properties of all samples (Figure 4). Wettability increases fastest for sample H, the only sample that achieved complete wetting after one hour of exposure. For the reference sample (denoted in Figure 4 as flat steel—“Flat St”) during this time, the values decreased insignificantly from 72° to 60°. Samples “K” and “J” demonstrated the best stability, maintaining hydrophobicity during 30 min of exposure. Sample “L” lost its superhydrophobicity after only 15 min and showed poor stability. Thus, the surfaces after spontaneous hydrophobization were vulnerable to ultraviolet irradiation. The samples containing bihierarchical LIPSS patterns in combination with microgrooves proved to be the most stable.

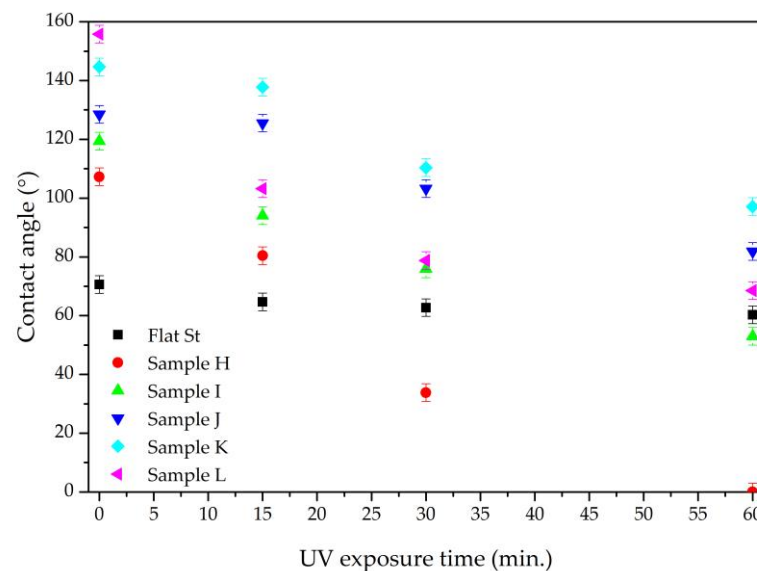
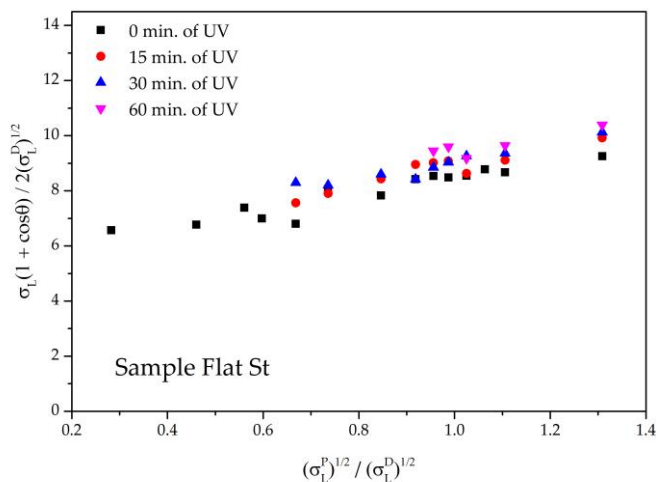


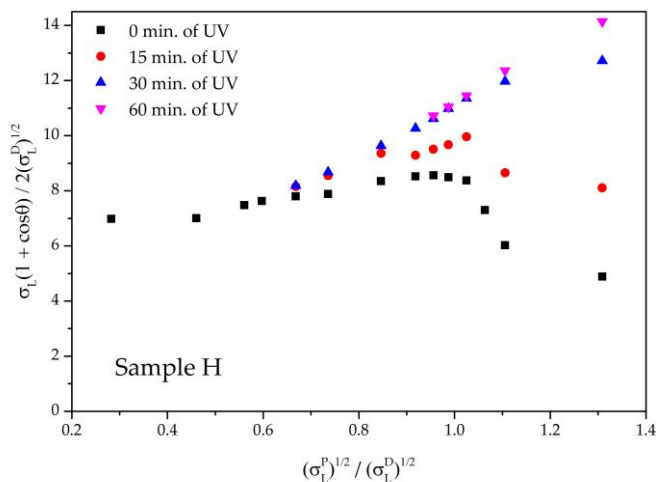
**Figure 4.** Water contact angle, depending on the duration of UV irradiation.

### 3.4. Wetting Samples with Liquids of Different Polarity and Owens–Wendt Plots

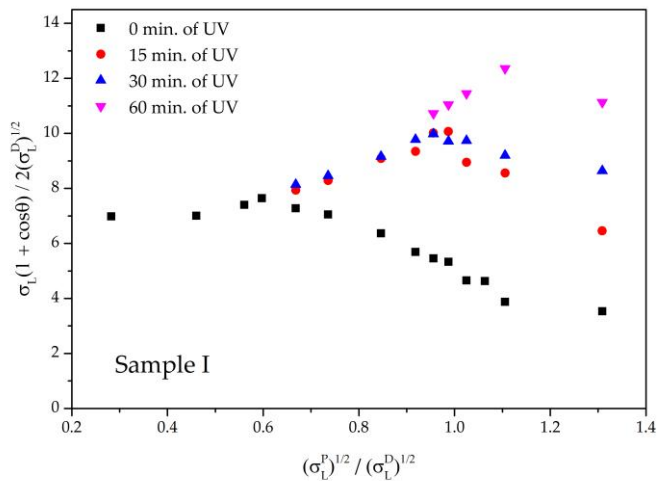
The Owens–Wendt plot of the reference surface (denoted in Figure 5a as flat steel—“Flat St”) can be approximated by a straight line, which makes it possible to determine the polar ( $\sigma_S^P = 5.8$  mN/m) and dispersive ( $\sigma_S^D = 33.6$  mN/m) components of the sample surface energy before UV irradiation. During aging,  $\sigma_S^D$  remained unchanged within the error, and the polar one increased to 8.5, 11.7, and 12.8 mN/m for 15, 30, and 60 min of UV exposure, respectively. This can be explained either by the oxidation of surface contaminants or by the thinning of their layer and the approach of a probe liquid droplet to the metal surface [48]. Similar processes can be expected for a textured surface (Figure 5b–f) when considering the increase in the specific surface (and, consequently, the ability to absorb contaminants) and the possible inhibition of some elements by the inner surface.



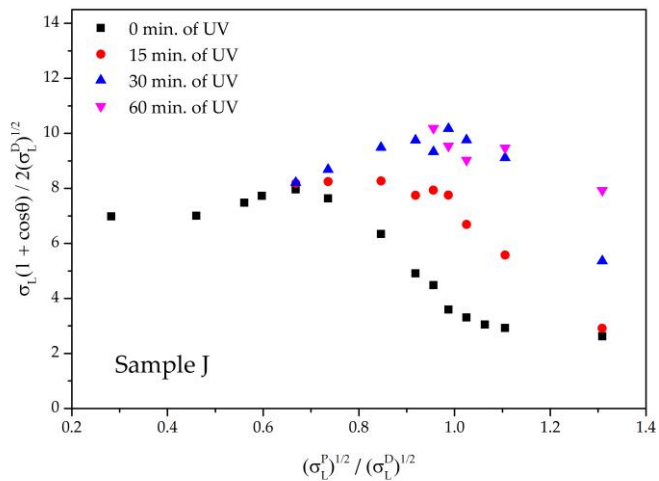
(a)



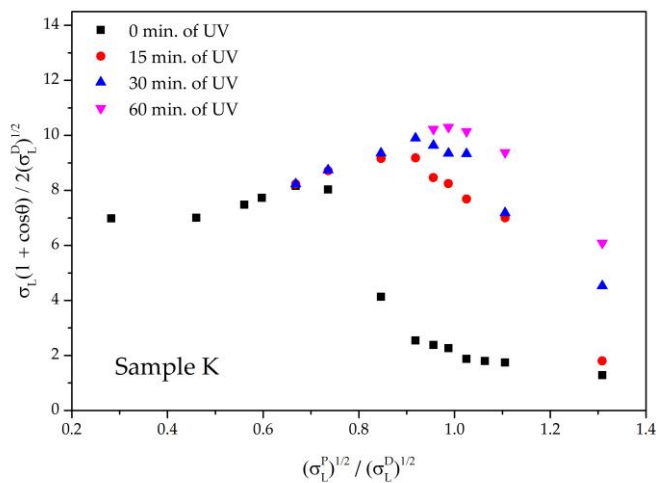
(b)



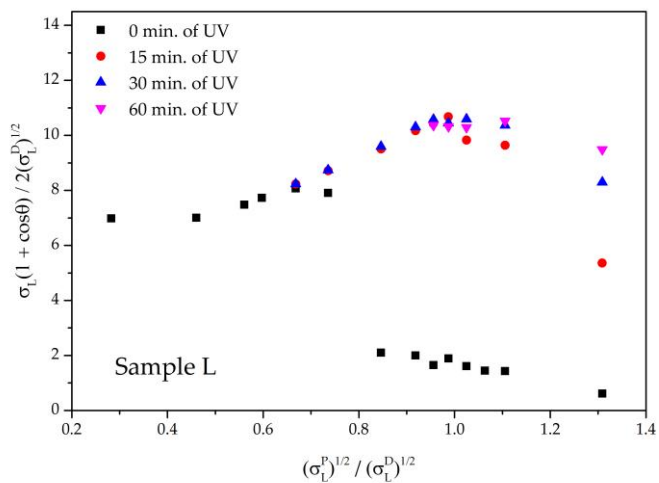
(c)



(d)



(e)



(f)

**Figure 5.** Owens–Wendt plots for samples with spontaneous hydrophobization under UV irradiation: (a) reference sample; (b) sample “H”; (c) sample “I”; (d) sample “J”; (e) sample “K”; and (f) sample “L”.

Sample “H”, containing only the LIPSS pattern, lost liquid repellency after 30 min of exposure to UV radiation, as seen from the “linearization” of the curve, indicating no wetting transition due to increased surface polarity. Its  $\sigma_S^P = 38.3$  mN/m, which makes the total surface energy close to that of water and, therefore, close to complete wetting by this probe liquid. For other surfaces, the linearization increased in the series K→J→L→I, which indicates the degree of surface stability of each sample to UV radiation. These changes are due to the same processes of transformation of the outer adsorption layer as in the case of the reference surface but are much more pronounced in terms of an increase in polarity and wettability. This can be explained by the fact that with a slight decrease in the intrinsic contact angle of the material according to the Cassie Equation (2), the fraction of the surface wetted by the liquid can increase significantly, and as a result,  $\cos\theta^*$  will decrease significantly.

A numerical description of the differences between these graphs is possible using the parameters of the characteristic curve:

1.  $\sigma_{TS}^D / \sigma_S^D$ —describes the ratio of the dispersion component of the texture surface energy ( $\sigma_{TS}^D$ ) to the dispersion component of the energy of the corresponding reference surface ( $\sigma_S^D = 33.6$  mN/m);
2.  $\sigma_L^P$ —equal to the minimum polar component of the surface energy of the probe liquid, which causes a wetting transition.

Both parameters are related to the topography and chemistry of the surface, but the second one is more sensitive to the polarity of the hydrophobizer layer [42]. However, the second parameter is quite difficult to determine from the Owens–Wendt plots in the case of significantly oxidized surfaces with increased wettability. Therefore, to characterize it, this paper proposes to use the position of the transition point from the curve to the linear form  $\sigma_{LIN}^P$ . The physical meaning of this point can be considered as the completion of the transient wetting process. At the same time, it would be wrong to state that the wetting of a textured surface is equivalent to the wetting of the corresponding reference surface due to the distortion introduced by the surface roughness in accordance with Wenzel’s Equation (1).

It can be noted that the parameter  $\sigma_{TS}^D / \sigma_S^D$  for textures increases under the action of UV radiation and makes it possible to numerically compare the resistance of textures to the action of this factor. The minimum value of the parameter before exposure corresponded to sample “L” (Table 4), but after 15 min, it was already higher than that of samples “J” and “K”, which indicates their greater stability. This was unexpected given that “L” contains more surface contaminants than “K”, as shown in Section 3.2. Sample “K” also had the lowest  $\sigma_{TS}^D / \sigma_S^D$  parameter at the end of the test, while sample “H”, which contained a pure LIPSS pattern, had the highest value.

**Table 4.** The  $\sigma_{TS}^D / \sigma_S^D$  parameters of textures.

Time, min	H	I	J	K	L
0	0.15	0.10	0.08	0.04	0.02
15	0.24	0.19	0.09	0.05	0.16
30	0.38	0.26	0.16	0.13	0.25
60	0.42	0.33	0.24	0.18	0.28

The change in the parameter  $\sigma_{LIN}^P$  with time for all textures (Table 5) indicates a significant increase in their wettability with respect to liquids with reduced surface tension. It is noteworthy that the initial value of the parameter  $\sigma_{LIN}^P$  for most of the samples (except for the sample “H”) was close, which can be explained by the similarity of the degradation processes of the organic layer. This parameter, as expected, increased with time, which was associated with surface hydrophilization. This process proceeded at approximately the same rate in all microstructured samples (slowest for samples “J” and “K”), except for sample “H”, containing the LIPSS pattern, for which hydrophilization occurred the

fastest. The slowest hydrophilization after an hour of UV irradiation was observed for the bihierarchical textures “J” and “K”.

**Table 5.** The  $\sigma_{LIN}^P$  parameters of textures.

Time, min	H	I	J	K	L
0	25.9	9.7	13.2	13.2	13.2
15	29.1	22.3	17.2	20.4	25.9
30	38.8	25.3	23.8	23.3	24.8
60	-	35.0	26.9	25.9	25.9

Thus, it has been shown that the organic layer formed during self-hydrophobization on the surface of textures after laser processing is unstable under UV irradiation. This could potentially be used to clean up such textures before post-treatment, but it points to problems when deploying spontaneously hydrophobized water-repellent surfaces outdoors. Nevertheless, to improve the stability of the hydrophobizer layer, one can switch from hydrocarbon chemistry to more stable organosilicon and organofluorine compounds. This will be one of the directions of our further research.

#### 4. Conclusions

It has been shown that the liquid repellency of spontaneously hydrophobized AISI 304 steel surfaces textured by femtosecond laser pulses is largely determined by their topography. In particular, LIPSS patterns showed surprisingly low liquid repellency compared to textures containing microgrooves. The non-polar surface layer on such a texture was sensitive to ultraviolet radiation and increased the polarity to a super-hydrophilic state. In addition to the radiation dose, the rate of such a transition was largely determined by the surface texture. It was demonstrated that the degradation rate was higher on surfaces containing LIPSS and lower on bihierarchical textures containing microgrooves. It has been shown that the Owens–Wendt method can be successfully used to compare the polarity of textured surfaces and, in particular, to compare their degradation rate under UV irradiation by comparing the  $\sigma_{TS}^D/\sigma_S^D$  and  $\sigma_{LIN}^P$  values from the plot.

**Author Contributions:** Conceptualization, O.M., D.B. and A.M.R.; methodology, O.M., D.B. and A.M.R.; validation, D.B. and O.M.; formal analysis, O.M. and D.B.; investigation, O.M. and D.B.; resources, O.M. and A.M.R.; data curation, D.B.; writing—original draft preparation, O.M. and D.B.; writing—review and editing, O.M., D.B. and A.M.R.; visualization, D.B.; supervision, O.M. and A.M.R.; project administration, O.M. and A.M.R.; funding acquisition, O.M. and A.M.R. All authors have read and agreed to the published version of the manuscript.

**Funding:** This research was funded by the Research Council of Lithuania, grant no. S-LU-22-3 and by the Ministry of Education and Science of Ukraine, reg. no. 0122U002645.

**Institutional Review Board Statement:** Not applicable.

**Informed Consent Statement:** Not applicable.

**Data Availability Statement:** Not applicable.

**Conflicts of Interest:** The authors declare no conflict of interest.

#### References

1. Ge-Zhang, S.; Yang, H.; Ni, H.; Mu, H.; Zhang, M. Biomimetic superhydrophobic metal/nonmetal surface manufactured by etching methods: A mini review. *Front. Bioeng. Biotechnol.* **2022**, *10*, 958095. [[CrossRef](#)]
2. Samanta, A.; Wang, Q.; Shaw, S.K.; Ding, H. Roles of Chemistry Modification for Laser Textured Metal Alloys to Achieve Extreme Surface Wetting Behaviors. *Mater. Des.* **2020**, *192*, 108744. [[CrossRef](#)]
3. Cai, Z.; Lin, J.; Hong, X. Transparent superhydrophobic hollow films (tshfs) with superior thermal stability and moisture resistance. *RSC Adv.* **2018**, *8*, 491–498. [[CrossRef](#)]
4. Hozumi, A.; Cheng, D.F.; Yagihashi, M. Hydrophobic/superhydrophobic oxidized metal surfaces showing negligible contact angle hysteresis. *J. Colloid Interface Sci.* **2011**, *353*, 582–587. [[CrossRef](#)] [[PubMed](#)]

5. Hsieh, C.T.; Chen, W.Y.; Wu, F.L. Fabrication and superhydrophobicity of fluorinated carbon fabrics with micro/nanoscaled two-tier roughness. *Carbon* **2008**, *46*, 1218–1224. [[CrossRef](#)]
6. He, S.; Zheng, M.; Yao, L.; Yuan, X.; Li, M.; Ma, L.; Shen, W. Preparation and properties of zno nanostructures by electrochemical anodization method. *Appl. Surf. Sci.* **2010**, *256*, 2557–2562. [[CrossRef](#)]
7. Meng, H.; Wang, S.; Xi, J.; Tang, Z.; Jiang, L. Facile means of preparing superamphiphobic surfaces on common engineering metals. *J. Phys. Chem. C* **2008**, *112*, 11454–11458. [[CrossRef](#)]
8. Syed, J.A.; Tang, S.; Meng, X. Super-hydrophobic multilayer coatings with layer number tuned swapping in surface wettability and redox catalytic anti-corrosion application. *Sci. Rep.* **2017**, *7*, 4403. [[CrossRef](#)]
9. Zhao, Y.; Tang, Y.; Wang, X.; Lin, T. Superhydrophobic cotton fabric fabricated by electrostatic assembly of silica nanoparticles and its remarkable buoyancy. *Appl. Surf. Sci.* **2010**, *256*, 6736–6742. [[CrossRef](#)]
10. Qi, D.; Lu, N.; Xu, H.; Yang, B.; Huang, C.; Xu, M.; Gao, L.; Wang, Z.; Chi, L. Simple approach to wafer-scale self-cleaning antireflective silicon surfaces. *Langmuir* **2009**, *25*, 7769–7772. [[CrossRef](#)]
11. Li, M.; Xu, J.; Lu, Q. Creating superhydrophobic surfaces with flowery structures on nickel substrates through a wet-chemical-process. *J. Mater. Chem.* **2007**, *17*, 4772. [[CrossRef](#)]
12. Wang, Y.; Wang, W.; Zhong, L.; Wang, J.; Jiang, Q.; Guo, X. Super-hydrophobic surface on pure magnesium substrate by wet chemical method. *Appl. Surf. Sci.* **2010**, *256*, 3837–3840. [[CrossRef](#)]
13. Erbil, H.Y. Practical applications of superhydrophobic materials and coatings: Problems and Perspectives. *Langmuir* **2020**, *36*, 2493–2509. [[CrossRef](#)] [[PubMed](#)]
14. Yuan, G.; Liu, Y.; Ngo, C.V.; Guo, C. Rapid Fabrication of Anti-Corrosion and Self-Healing Superhydrophobic Aluminum Surfaces through Environmentally Friendly Femtosecond Laser Processing. *Opt. Express* **2020**, *28*, 35636. [[CrossRef](#)]
15. Ta, V.D.; Dunn, A.; Wasley, T.J.; Li, J.; Kay, R.W.; Stringer, J.; Smith, P.J.; Esenturk, E.; Connaughton, C.; Shephard, J.D. Laser Textured Superhydrophobic Surfaces and Their Applications for Homogeneous Spot Deposition. *Appl. Surf. Sci.* **2016**, *365*, 153–159. [[CrossRef](#)]
16. Zinnecker, V.; Madden, S.; Stokes-Griffin, C.; Compston, P.; Rode, A.V.; Rapp, L. Ultrashort pulse laser ablation of steel in ambient air. *Opt. Laser Technol.* **2022**, *148*, 107757. [[CrossRef](#)]
17. Winter, J.; Spellaugue, M.; Hermann, J.; Eulenkamp, C.; Huber, H.P.; Schmidt, M. Ultrashort single-pulse laser ablation of stainless steel, aluminium, copper and its dependence on the pulse duration. *Opt. Express* **2021**, *29*, 14561. [[CrossRef](#)]
18. Yong, J.; Yang, Q.; Guo, C.; Chen, F.; Hou, X. A Review of Femtosecond Laser-Structured Superhydrophobic or Underwater Superoleophobic Porous Surfaces/Materials for Efficient Oil/Water Separation. *RSC Adv.* **2019**, *9*, 12470–12495. [[CrossRef](#)]
19. Indrišiūnas, S.; Svirplys, E.; Gedvilas, M. Large-area fabrication of LIPSS for wetting control using multi-parallel femtosecond laser processing. *Materials* **2022**, *15*, 5534. [[CrossRef](#)]
20. Sun, H.; Li, J.; Liu, M.; Yang, D.; Li, F. A Review of Effects of Femtosecond Laser Parameters on Metal Surface Properties. *Coatings* **2022**, *12*, 1596. [[CrossRef](#)]
21. Florian, C.; Skoulas, E.; Puerto, D.; Mimidis, A.; Stratakis, E.; Solis, J.; Siegel, J. Controlling the wettability of steel surfaces processed with femtosecond laser pulses. *ACS Appl. Mater. Interfaces.* **2018**, *10*, 36564–36571. [[CrossRef](#)] [[PubMed](#)]
22. Zhidkov, M.V.; Vershinina, T.N.; Golosova, O.A.; Kudryashov, S.I.; Ionin, A.A. Surface texturing of steel by femtosecond laser and accompanying structure/phase transformations. *Opt. Laser Technol.* **2020**, *131*, 106370. [[CrossRef](#)]
23. Long, J.; Pan, L.; Fan, P.; Gong, D.; Jiang, D.; Zhang, H.; Li, L.; Zhong, M. Cassie-State Stability of Metallic Superhydrophobic Surfaces with Various Micro/Nanostructures Produced by a Femtosecond Laser. *Langmuir* **2016**, *32*, 1065–1072. [[CrossRef](#)] [[PubMed](#)]
24. Yong, J.; Yang, Q.; Hou, X.; Chen, F. Nature-Inspired Superwettability Achieved by Femtosecond Lasers. *Ultrafast Sci.* **2022**, *2022*, 1–51. [[CrossRef](#)]
25. Sun, L.; Yuan, G.; Gao, L.; Yang, J.; Chhowalla, M.; Gharahcheshmeh, M.H.; Gleason, K.K.; Choi, Y.S.; Hong, B.H.; Liu, Z. Chemical vapour deposition. *Nat. Rev. Methods Primers* **2021**, *1*, 5. [[CrossRef](#)]
26. Shadmani, S.; Khodaei, M.; Chen, X.; Li, H. Superhydrophobicity through coatings prepared by chemical methods. In *Superhydrophobic Surfaces—Fabrications to Practical Applications*; IntechOpen: London, UK, 2020. [[CrossRef](#)]
27. Emelyanenko, K.A.; Emelyanenko, A.M.; Boinovich, L.B. Laser Obtained Superhydrophobic State for Stainless Steel Corrosion Protection, a Review. *Coatings* **2023**, *13*, 194. [[CrossRef](#)]
28. Martínez-Calderon, M.; Rodríguez, A.; Dias-Ponte, A.; Morant-Miñana, M.C.; Gómez-Aranzadi, M.; Olaizola, S.M. Femtosecond Laser Fabrication of Highly Hydrophobic Stainless Steel Surface with Hierarchical Structures Fabricated by Combining Ordered Microstructures and LIPSS. *Appl. Surf. Sci.* **2016**, *374*, 81–89. [[CrossRef](#)]
29. Elleb, R.; Engel, T.; Antoni, F.; Fontaine, J.; Mermet, F.; Poncin-Epaillard, F. Study of Femtosecond Laser Multi-Scale Textured Steel Surfaces on the Wettability in Relation to Aging. *J. Mater. Sci.* **2021**, *56*, 20169–20180. [[CrossRef](#)]
30. Zhang, Y.; Jiao, Y.; Li, C.; Chen, C.; Li, J.; Hu, Y.; Wu, D.; Chu, J. Bioinspired micro/nanostructured surfaces prepared by femtosecond laser direct writing for multi-functional applications. *Int. J. Extreme Manuf.* **2020**, *2*, 032002. [[CrossRef](#)]
31. Kietzig, A.M.; Hatzikiriakos, S.G.; Englezos, P. Patterned Superhydrophobic Metallic Surfaces. *Langmuir* **2009**, *25*, 4821–4827. [[CrossRef](#)]
32. Kietzig, A.M.; Mirvakili, N.M.; Kamal, S.; Englezos, P.; Hatzikiriakos, S.G. Laser-patterned super-hydrophobic pure metallic substrates: Cassie to Wenzel Wetting Transitions. *J. Adhes. Sci. Technol.* **2011**, *25*, 2789–2809. [[CrossRef](#)]

33. Basset, S.; Heisbourg, G.; Pascale-Hamri, A.; Benayoun, S.; Valette, S. Effect of Texturing Environment on Wetting of Biomimetic Superhydrophobic Surfaces Designed by Femtosecond Laser Texturing. *Nanomaterials* **2022**, *12*, 3099. [[CrossRef](#)]
34. Bizi-bandoki, P.; Valette, S.; Audouard, E.; Benayoun, S. Time Dependency of the Hydrophilicity and Hydrophobicity of Metallic Alloys Subjected to Femtosecond Laser Irradiations. *Appl. Surf. Sci.* **2013**, *273*, 399–407. [[CrossRef](#)]
35. Fürbacher, R.; Liedl, G.; Otto, A. Fast Transition from Hydrophilic to Superhydrophobic, Icephobic Properties of Stainless Steel Samples after Femtosecond Laser Processing and Exposure to Hydrocarbons. *Procedia CIRP* **2022**, *111*, 643–647. [[CrossRef](#)]
36. Becker, S.; Merz, R.; Hasse, H.; Kopnarski, M. Solvent Cleaning and Wettability of Technical Steel and Titanium Surfaces. *Adsorpt. Sci. Technol.* **2016**, *34*, 261–274. [[CrossRef](#)]
37. Deflorian, F.; Rossi, S.; Fedel, M. Organic coatings degradation: Comparison between natural and artificial weathering. *Corros. Sci.* **2008**, *50*, 2360–2366. [[CrossRef](#)]
38. Prydatko, A.; Myronyuk, O.; Svidersky, V. Analysis of approaches to mathematical description of the characteristics of materials with high hydrophobicity. *East. Eur. J. Enterp. Technol.* **2015**, *5*, 30. [[CrossRef](#)]
39. Zhang, B.X.; Cai, Z.H.; Ding, Q.; Zhu, K.Q.; Yang, Y.R.; Wang, X.D. Bouncing Dynamics of nanodroplets impacting superhydrophobic surfaces: The coupling influence of wetting transitions and scale effects. *Colloids Surf. A Physicochem. Eng. Asp.* **2023**, *657*, 130579. [[CrossRef](#)]
40. Binali, R.; Demirpolat, H.; Kuntoğlu, M.; Salur, E. Different Aspects of Machinability in Turning of AISI 304 Stainless Steel: A Sustainable Approach with MQL Technology. *Metals* **2023**, *13*, 1088. [[CrossRef](#)]
41. Pańcikiewicz, K.; Świerczyńska, A.; Hučko, P.; Tumidajewicz, M. Laser Dissimilar Welding of AISI 430F and AISI 304 Stainless Steels. *Materials* **2020**, *13*, 4540. [[CrossRef](#)]
42. Myronyuk, O.; Baklan, D.; Rodin, A.M.; Vanagas, E.; Yong, Z. Owens–Wendt Characterization of Femtosecond-Laser-Textured Hydrophobic Aluminum Surfaces. *Coatings* **2023**, *13*, 1104. [[CrossRef](#)]
43. Myronyuk, O.; Baklan, D.; Vasilyev, G.S.; Rodin, A.M.; Vanagas, E. Wetting Patterns of Liquid-Repellent Femtosecond Laser Textured Aluminum Surfaces. *Coatings* **2022**, *12*, 1852. [[CrossRef](#)]
44. Zhang, Z.; Wang, W.; Korpacz, A.N.; Dufour, C.R.; Weiland, Z.J.; Lambert, C.R.; Timko, M.T. Binary Liquid Mixture Contact-Angle Measurements for Precise Estimation of Surface Free Energy. *Langmuir* **2019**, *35*, 12317–12325. [[CrossRef](#)] [[PubMed](#)]
45. Owens, D.K.; Wendt, R.C. Estimation of the Surface Free Energy of Polymers. *J. Appl. Polym. Sci.* **1969**, *13*, 1741–1747. [[CrossRef](#)]
46. Wu, B.; Zhou, M.; Li, J.; Ye, X.; Li, G.; Cai, L. Superhydrophobic Surfaces Fabricated by Microstructuring of Stainless Steel Using a Femtosecond Laser. *Appl. Surf. Sci.* **2009**, *256*, 61–66. [[CrossRef](#)]
47. Zeman, A.; Novotny, R.; Uca, O.; Krsjak, V.; Macak, J.; Debarberis, L. Behavior of cold-worked AISI-304 steel in stress-corrosion cracking process: Microstructural aspects. *Appl. Surf. Sci.* **2008**, *255*, 160–163. [[CrossRef](#)]
48. Somlyai-Sipos, L.; Baumli, P. Wettability of Metals by Water. *Metals* **2022**, *12*, 1274. [[CrossRef](#)]

**Disclaimer/Publisher’s Note:** The statements, opinions and data contained in all publications are solely those of the individual author(s) and contributor(s) and not of MDPI and/or the editor(s). MDPI and/or the editor(s) disclaim responsibility for any injury to people or property resulting from any ideas, methods, instructions or products referred to in the content.